Open Research Online

The Open University's repository of research publications
and other research outputs

Evolution and impact of defects in a p-channel CCD after cryogenic proton-irradiation

Journal Item

oro.open.ac.uk

Evolution and Impact of Defects in a p-Channel CCD After Cryogenic Proton-Irradiation

Daniel Wood, David J. Hall, Jason Gow, Jesper Skottfelt, Neil J. Murray,
Konstantin Stefanov, and Andrew D. Holland

Abstract— The p-channel charge coupled devices (CCDs) have been shown to display improved tolerance to radiation-induced charge transfer inefficiency when compared with n-channel CCDs. However, the defect distribution formed during irradiation is expected to be temperature dependent due to the differences in lattice energy caused by a temperature change. This has been tested through defect analysis of two p-channel e2v CCD204 devices, one irradiated at room temperature and one at a cryogenic temperature (153 K). Analysis is performed using the method of single trap pumping. The dominant charge trapping defects at these conditions have been identified as the donor level of the silicon divacancy and the carbon interstitial defect. The defect parameters are analyzed both immediately postirradiation and following several subsequent room-temperature anneal phases up until a cumulative anneal time of approximately 10 months. We have also simulated charge transfer in an irradiated CCD pixel using the defect distribution from both the room-temperature and cryogenic case, to study how the changes affect imaging performance. The results demonstrate the importance of cryogenic irradiation and annealing studies, with large variations seen in the defect distribution when compared to a device irradiated at room-temperature, which is the current standard procedure for radiation-tolerance testing.

Index Terms— Carbon, charge coupled devices (CCDs), defect, divacancy, p-channel, pocket pumping, radiation damage, trap pumping.

I. INTRODUCTION

RADIATION-INDUCED defects are responsible for charge-transfer performance degradation in charge coupled devices (CCDs) because they introduce stable deep-levels within the silicon band-gap, which are capable of trapping a single charge carrier (h^+ for the p-channel case) for a length of time before emission [1]. This time is heavily temperature dependent and is defined as the defect emission time-constant (τ_e). Where the emission time-constant at a given temperature is close to the line transfer time of the CCD,

charge carriers can be moved efficiently between adjacent charge-packets, leading to image smearing [2] which is detrimental to the science goals of the detector [3].

The p-channel CCDs have demonstrated improved tolerance to radiation damage induced image degradation because the predominant defects produced, which are the donor level of the silicon divacancy and the carbon interstitial defect, both have emission time-constants which interfere less with the typical CCD operating conditions at nominal space-based detector temperatures than in the n-channel case [4]. These two defects have been studied extensively with the donor level of the divacancy established as having an energy level of around $E_v + 0.20$ eV [5]–[7] and the carbon interstitial an energy level of $E_v + 0.27$ eV [8], [9].

However, previous studies have also shown considerable uncertainty in the defect emission time-constants, of up to an order of magnitude [10]. It is therefore vital both for a complete comparison between n- and p-channel CCDs and for future mitigation of radiation-induced charge transfer inefficiency (CTI) to study with high precision the parameters of defects produced in p-type silicon postirradiation. Another important factor to account for is the device temperature during irradiation, as this affects the lattice energy and therefore the defect formation and interaction rates. An initial analysis of the effect of temperature was carried out in [11] and showed considerable differences in the initial defect distributions, as well as following a room-temperature anneal of up to approximately 1 month. Here we continue this analysis to investigate the longer term effects of such an irradiation as well as the potential impact on device performance.

II. TRAP PUMPING

The charge trapping process is described by Shockley-Read-Hall kinetics [12], [13] which models the capture and release of electrons (or holes) through the use of two exponential time constants; the capture time-constant and emission time-constant, as shown in (1) and (2). These contain terms for the thermal velocity of a hole and the effective density of states in the valence band, as given in (3) and (4). Here σ is the cross section, n is the electron concentration at the trap location, E is the energy of the level above the valence band edge and $m^*_{\text{DOS,Con}}$ are the effective hole masses for density of states and conductivity calculations, respectively. The probability of capture or emission before a given time t is then given by (5)

$$\tau_c = \frac{1}{\sigma n v_{\text{th}}} \tag{1}$$

$$\tau_e = \frac{1}{\sigma N_v v_{\text{th}}} \exp\left(\frac{E}{kT}\right) \qquad (2)$$

$$N_v = 2\left(\frac{2\pi m_{\text{DOS}}^* kT}{h^2}\right)^{\frac{3}{2}} \qquad (3)$$

$$v_{\text{th}} = \sqrt{\frac{3kT}{m_{\text{Con}}^*}} \qquad (4)$$

$$P_{c,e} = 1 - \exp\left(\frac{-t}{\tau_{c,e}}\right). \qquad (5)$$

As previously stated the emission time-constant is the defect parameter which governs how destructive the defect can be to charge transfer performance. At the signal levels used throughout this paper it is acceptable to assume instant capture, i.e., the capture time constant is much smaller than the dwell time for which the signal is under each phase [14]. This is because the signal charge cloud is large enough that it can encounter an empty trap state almost instantly.

To analyze the defect emission time-constants the method of trap pumping is used, which is described fully in [14] and [15]. The technique works by clocking signal charge from beneath an initial collecting phase electrode to beneath the same electrode in the next pixel, and back again. This is repeated over a number of cycles. For a defect beneath a barrier phase electrode there exists a probability per cycle of carrier capture from one charge packet and release into an adjacent charge packet. This is defined as the probability of pumping [shown in (6)] and depends on the emission time constant of the responsible defect as well as the time period t_{ph} (labeled as the phase time) between each charge transfer

$$P_p = \exp\left(\frac{-t}{\tau_e}\right) - \exp\left(\frac{-2t}{\tau_e}\right). \qquad (6)$$

If the probability is large enough then over a number of cycles N an image will be produced containing a signal dipole at the corresponding pixel; where a pixel significantly darker than the average background level neighbors a pixel significantly brighter, or vice-versa. The intensity of this signal dipole is defined as $I = N \times P_p$. Differentiation of the expression for signal dipole intensity with respect to phase time gives an expression relating the phase time at maximum intensity to the emission time constant of the underlying defect. Therefore by analyzing the intensity of such dipoles with varying t_{ph} we can probe the emission time constant of individual defects.

The technique also allows for analysis of defect energy levels if the process can be performed at a number of different temperatures. Since pocket pumping shows individual defect locations within the device, the emission time constant of a given defect can be tracked with changing temperature. Plotting tau(e) against T allows for a fit based on (2). Pocket pumping is therefore a powerful technique for defect analysis; specifically as it allows for the study of individual defects as opposed to the average effects of many defects as seen in techniques such as DLTS [16].

III. CRYOGENIC IRRADIATION

Using the trap pumping method we have analyzed the defects produced in a p-channel CCD204 following irradiation
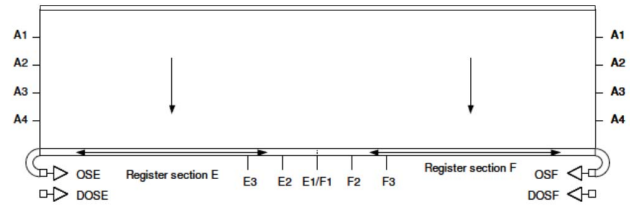

Fig. 1. Schematic of the e2v CCD204 showing the direction of charge transfer and the spilt serial register.

with protons at cryogenic temperature (153 K). Results from a room-temperature proton irradiation of a CCD204 were used for comparison and to identify the most probable defect distribution postirradiation. Under the conditions of this paper two defect species dominate charge-transfer degradation; a donor level of the silicon divacancy ($VV^{+/0}$) and the carbon interstitial defect (C_i) [10].

Measurements were performed at 153-K postirradiation and then subsequently after periods of approximately 1 day, 1 week, 1 month, 3 months, and 10 months at room-temperature.

The e2v CCD204 is a 4 k × 1 k device which utilizes a split output register with two separate output nodes. This device is a development chip toward the Euclid CCD273, with similar pixel architecture. The CCD204 has 12-μm square pixels and a channel width of 50 μm. A schematic of the CCD204 is shown in Fig. 1. For this paper two p-channel CCD204 devices were irradiated at the Synergy Health 5MV Tandem Accelerator (U.K.) [17].

One device was held at room-temperature during irradiation and received a 10-MeV equivalent proton fluence of 2×10^9 cm^{-2}. A second device was held at cryogenic temperature (153 K) and received a 10-MeV equivalent fluence of 1.24×10^9 cm^{-2}. The irradiated regions were chosen such as to leave the output nodes unirradiated. Full details of the irradiation are outlined in [17]. All devices were held at 153 K when not being tested or annealed. All of the results presented here have been scaled to the fluence received by the cryogenically irradiated device.

A cryogenic irradiation was performed in order to more closely mirror the conditions in a typical space-based detector as impinging particles strike the CCD and to monitor the effect this has on the defect distribution which is formed. The room-temperature irradiation results provided a start point for a comparison between the defect distributions formed in each temperature case.

Defect emission time-constant distributions immediately postirradiation for both the room-temperature and cryogenically irradiated devices are presented in [11]. The initial defect distribution at 153 K of the room-temperature irradiated device is shown in Fig. 2(a). Initial results from this device showed the donor level of the divacancy to be by far the most abundant defect produced, with a dominant peak in the emission time constant distribution at 30 μs. Slower defects are also present but there is no clear second peak in the distribution corresponding to another defect species. The defect emission time constant distribution formed in the
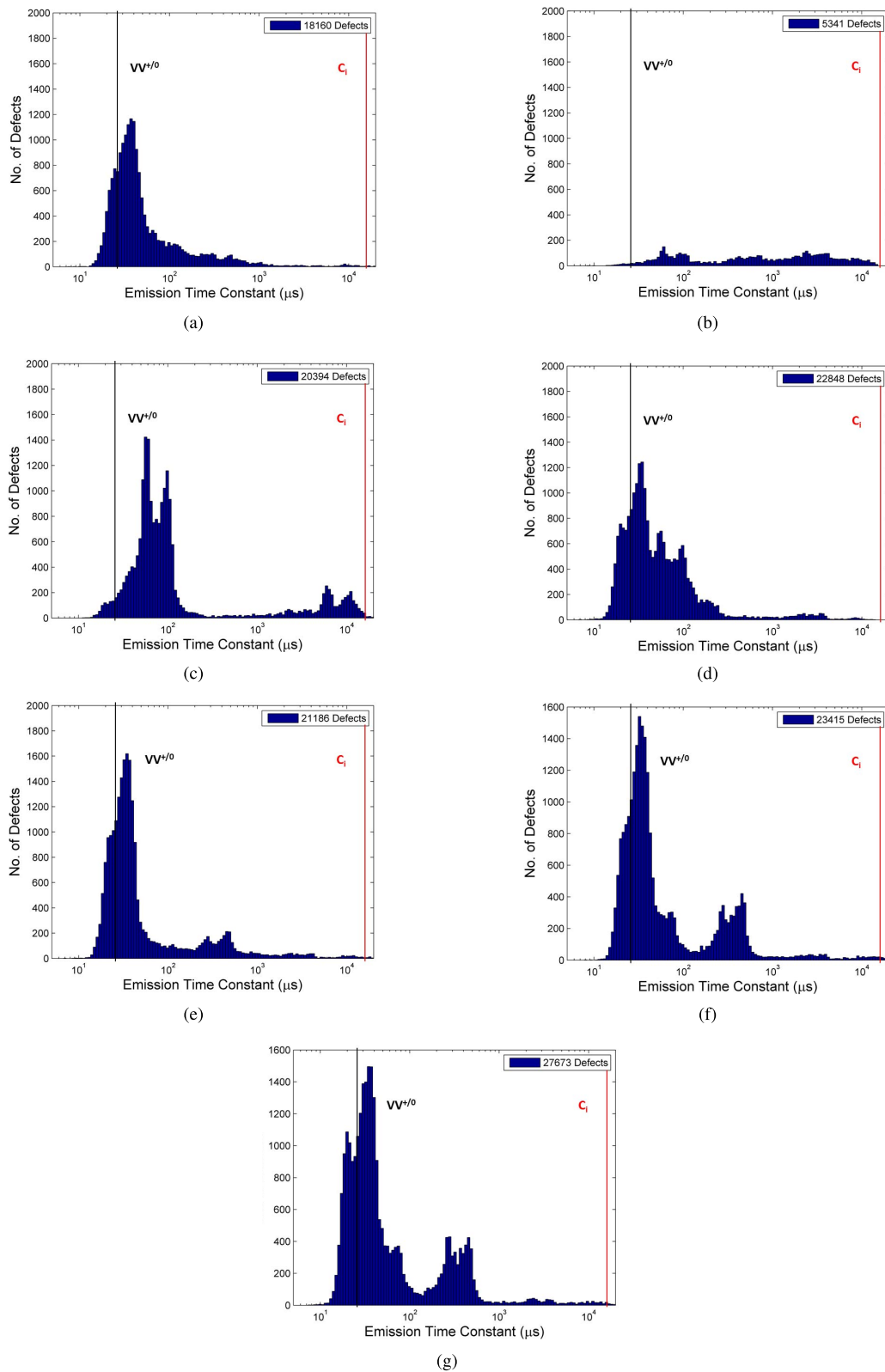
Fig. 2. Defect emission time-constant distributions for both devices at various stages throughout the study. All testing were carried out at 153 K. Each anneal stage was performed at room-temperature. (a) Room-temperature irradiated device. Included for reference are the literature value lines for the two defects of relevance at 153 K [10]. (b) Cryogenically irradiated device, immediately postirradiation. (c) Cryo device following 1-day anneal. (d) Cryo device following 1-week anneal. (e) Cryo device following 1-month anneal. (f) Cryo device following 3-month anneal. (g) Cryo device following 10-month anneal.

room-temperature irradiated device also shows a large spread around the main peak; with a mean emission time constant of approximately 40 ± 20 μs at full width-half maximum

(using the nonscaled distribution). The spread is therefore around 50% and relates well to the large emission time constant uncertainties seen in [10]. However, using the method of

trap pumping has allowed for the analysis of individual defect emission time constants with low (approximately 5% [11]) and therefore it is determined that for the case of defects in a CCD the majority of this spread is a genuine and may arise from small fluctuations in temperature, electric field or other local effects such as stress. Another possible explanation is different orientations of the same defect within the lattice.

Initial results from the cryogenic device are shown in Fig. 2(b) and show far fewer defects produced than in the room-temperature case. Although a small peak in the emission time constant distribution is present at typical divacancy range there is no clearly identifiable defect species present in large numbers.

Following analysis of the initial distributions a trap pumping method with a lower temporal resolution was used on the cryogenic device so that the technique could be run over a shorter period of time, allowing for study of the defect evolution in the first few hours after irradiation. The defect distribution was reanalyzed every few hours over a period of several days until the first room-temperature anneal stage, with the number of divacancy defects tracked over time. The results are presented in [11] and are shown here in Fig. 3(a).

For the first few days after irradiation there are small variations in the number of defects found, showing that the situation is still dynamic. This is shown more clearly in Fig. 3(b) which is simply a zoomed in view of the initial hours from Fig. 3(a). Defects may be mobile or able to disassociate/recombine even at cryogenic temperatures. Changes are still visible right up until the point of the first anneal stage, at around 120 h after irradiation. The device was annealed for 26 h at room-temperature before being cooled back down to 153 K for testing. Immediately obvious is the large increase in the number of divacancy defects found after anneal, with the defect distribution more closely resembling the room-temperature device at this stage.

IV. ANNEALING

Several room-temperature anneal stages were carried out resulting in a cumulative anneal time of approximately 10 months. A major advantage of trap pumping is the ability to identify individual defects which are present after each anneal stage and to monitor their emission time constants, energy levels and capture cross sections on an individual basis [14]. The large number of defects present gives good statistics and therefore a highly accurate calculation of defect parameters.

A trap-pumping analysis of the cryogenic device was carried out after each anneal stage, producing the defect emission time-constant distribution for the nominal testing temperature of 153 K. Results up until a total anneal time of 1 month were presented in [11], here we also include additional stages after total anneal times of approximately 3 and 10 months. Further analysis was completed at several temperatures between 143–173 K at each anneal stage where the data was available. The temperature dependence of the emission time constant [see (2)] allows for a calculation of the defect energy level as outlined in the earlier trap pumping section. This can be
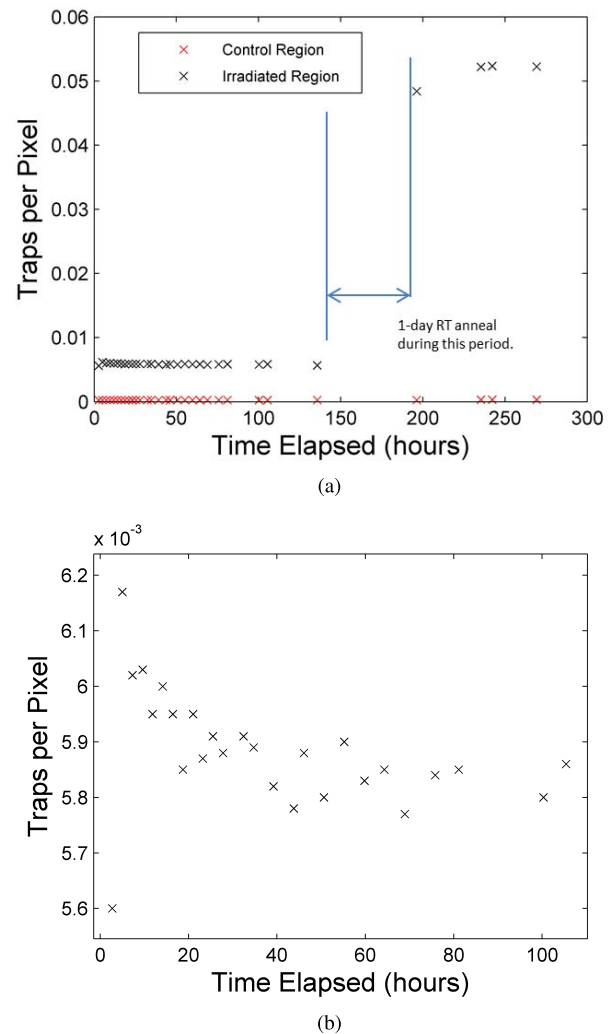

(a)

(b)

Fig. 3. Divacancy defects per pixel found in the cryogenically irradiated device postirradiation using the trap-sweeping method. (a) Divacancy defects per pixel against time elapsed since irradiation, for the cryogenically irradiated device. Includes the 1-day anneal stage as specified. (b) Zoomed in view of the first 120 h after irradiation showing that there are small variations while the device remains cold. Note the anomalous first datapoint, showing a reduced number of defects. The reason for this lower value is unknown but it could be that some defects had not yet stabilized within the lattice since the situation remains dynamic long after irradiation.

used to identify the defect species present and confirm the time constant data.

Emission time constant distributions for all fit defects at 153 K following each anneal stage are shown in Fig. 2(c)–(g). Each shows a large peak around the expected divacancy emission time constant; however, the situation is dynamic, with the divacancy distribution being non-Gaussian and containing two or more discernible peaks. From these distributions it appears as though many of the defects are moving and/or reorienting over these time scales, and that the overall defect distribution is tending toward the room-temperature case, i.e., divacancy dominated with a second slower defect species corresponding to the carbon interstitial. The total number of defects found within our time range shows an increase over time even at the final stage tested, showing that the distribution is still changing after this length of time.
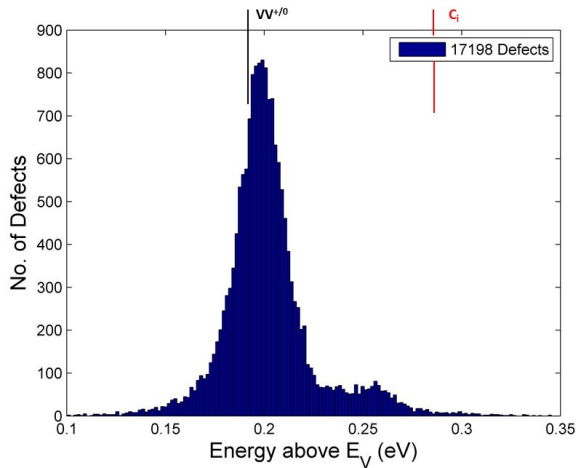
Fig. 4. Energy distribution for all fit defects found at 143, 148, and 153 K after the 1-month room-temperature anneal stage. The distribution of energies originates from calculating the energy level of each individual defect based on time-constant measurements, for which the measurement uncertainty is small (approximately 5%). This uncertainty is negligible compared to the width of the distribution. Also shown for comparison are the energies taken from [10].

Following the further testing at several temperatures between 143–173 K, defect energy levels were calculated for all defects which appear at every temperature. The energy distribution for the 1-day anneal stage was presented in [11] and showed two defect species consistent with the divacancy donor level and the carbon interstitial. Here the 1-month stage has been analyzed, Fig. 4, since this more closely resembles the final distribution Defects included are those which were found when testing at 143, 148, and 153 K. The results do not differ appreciably from the values found at the 1-day anneal stage. We find for the large peak an energy level of $E_v + 0.20(\pm 0.02)$ eV which is consistent with the value of $E_v + 0.19$ eV found by Mostek *et al.* [10] and earlier DLTS studies [5]–[7] for the divacancy donor level.

The smaller peak contains fewer defects and is distorted slightly by the spread from the much larger divacancy peak, but shows an approximate Gaussian energy distribution with an energy level of $E_v + 0.26(\pm 0.02)$ eV. This is also consistent within uncertainties with the value of $E_v + 0.28$ eV found by Mostek *et al.* [10] and earlier DLTS studies for the carbon interstitial level [8]–[10]. It should be noted, however, that previous studies have considered the overall effects of many defects, whereas the values quoted in this paper come from the distributions of individually analyzed defects, on which the measurement uncertainty is negligible compared to the width of the overall distribution.

We therefore believe that as expected the two defect species of interest are the donor level of the divacancy and the carbon interstitial. The energy distributions do not show any other noticeable peaks, which imply no other stable defect species are involved that can be detected. Therefore, the separate time-constant peaks seen for both the divacancy and the carbon interstitial most probably relate to different orientations of the same defect. It is clear from the defect densities, locations, and time-constants that there are large changes occurring in the defect distributions over these time scales at room-temperature.

Here we have seen that the effect of a room-temperature anneal on the defect distribution formed in a cryogenically irradiated device is significant and irreversible. Therefore a vital element of further work in this area is to study a device irradiated cryogenically and maintained at this temperature, such as a device would experience in space. It may be that given sufficient time the defects in both the room-temperature and cryogenically irradiated devices will reach the same final distribution. However, for the cryogenic case it may be that the lattice does not have enough energy for some processes to take place and so it could be that the final distributions diverge in each case. Further analysis of such devices is required both for improved understanding of the damage process and better context regarding device performance in a space environment.

V. CHARGE TRANSFER SIMULATIONS

As shown in Fig. 1, the initial defect distribution differs greatly between the device irradiated at room-temperature and the device irradiated at 153 K. It is therefore expected that there will be differences in the imaging performance of the two devices. To investigate this a Monte Carlo model of charge transfer in a radiation damaged CCD was used to simulate the effects of each defect distribution. The specific model used was the Open University Monte Carlo model (OUMC) which is described in [18]. The OUMC allows for the direct input of device specific electron density simulations and therefore does not require analytical assumptions about charge cloud density. The model can also take as an input a distribution of individual defect emission time constants; allowing for the defect distributions which have been found in each device through trap pumping to be analyzed directly. A reduced number of defects was used for the device irradiated at room-temperature to account for the higher fluence received by this device.

For this paper, the OUMC modeled the effect of the two different defect distributions on charge transfer in a Euclid pixel (CCD273). Since the analyzed region of each device was 400 rows by 600 columns, charge transfer was modeled using 400 parallel transfers and 600 serial transfers where appropriate. A single parallel shift consists of four steps $t_{ph} = [t_{dwell} + t_{shift}, t_{shift}, t_{shift}, t_{shift}]$ where t_{dwell} is the time taken to read out the serial register, and t_{shift} is the time between each phase shift [18]. Two different parallel clocking schemes were simulated; a short scheme $[0.03313, 2.84 \times 10^{-5}, 2.84 \times 10^{-5}, 2.84 \times 10^{-5}]$ s and a long scheme $[0.0361, 0.003, 0.003, 0.003]$ s. The serial transfer time is 4.77×10^{-6} s.

The first test uses an initial 5-pixel block of 400 electrons signal. The defect capture time is instantaneous for all defects, in order to simulate the realistic case where the capture time constant is much less than the dwell time. The first pixel response (FPR) and extended pixel edge response (EPER) are modeled after charge transfer simulations in three separate cases; the parallel short clocking scheme, the parallel long clocking scheme and the serial clocking scheme. The results are shown in Fig. 4.

For the long parallel scheme there is only a small amount of deferred charge for both the room-temperature and cryogenic
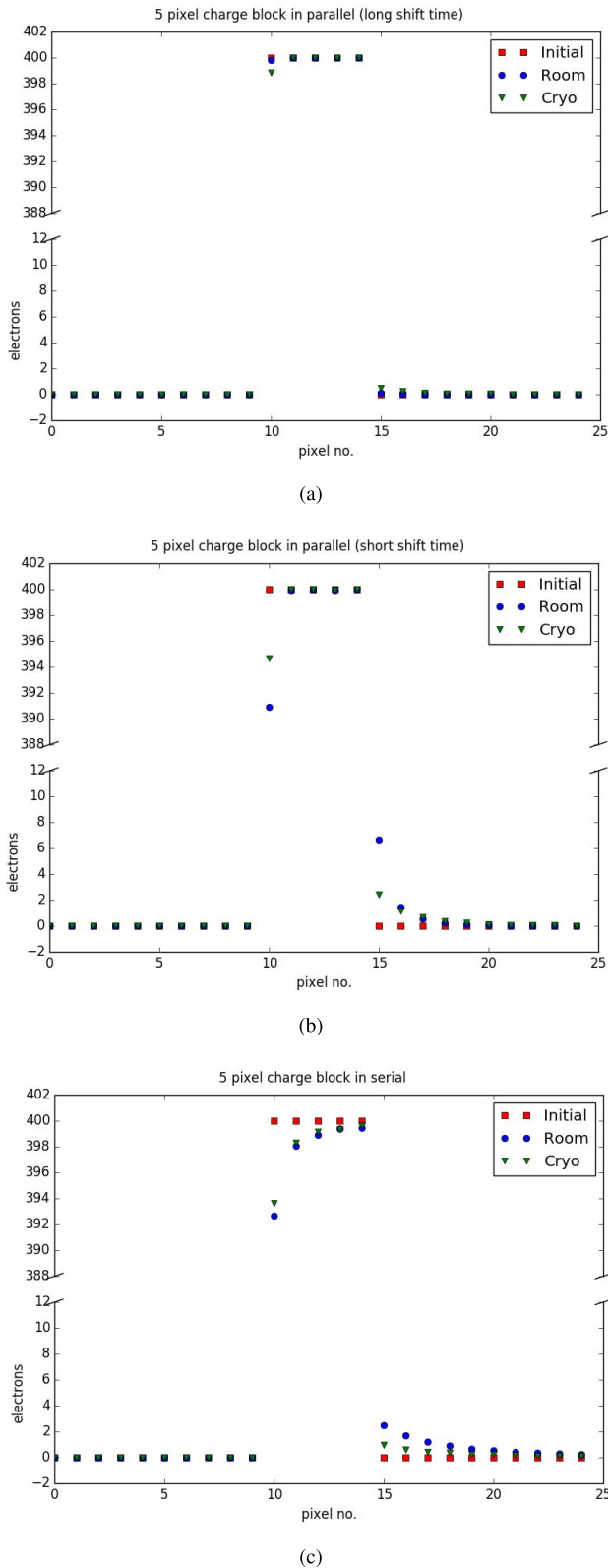
(a)

(b)

(c)

Fig. 5. FPR and EPER simulation results for a 5-pixel block of charge transferred using 400 parallel transfers for each clocking scheme and 600 serial transfers. Note the discontinuity in the *y*-axis. (a) Long parallel clocking scheme. (b) Short parallel clocking scheme. (c) Serial clocking scheme.
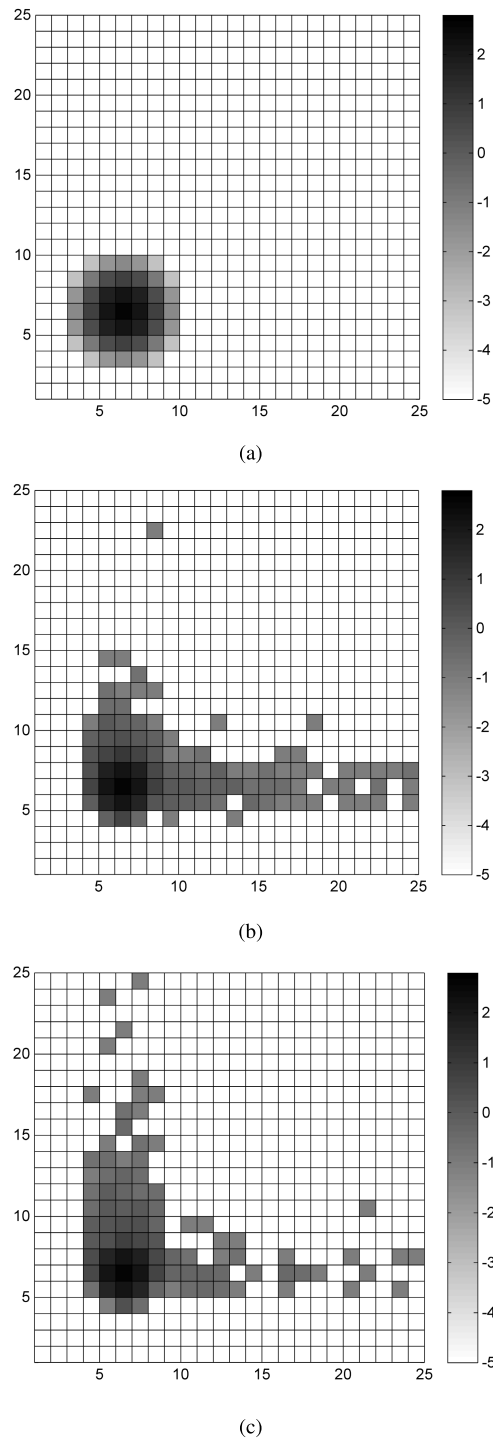

(a)

(b)

(c)

Fig. 6. Simulation results for a Gaussian point source given 400 parallel and 600 serial transfers using both the room-temperature and cryogenic defect distributions. (a) Inital point source. (b) Point source after transfer using the room-temperature defect distribution. (c) Point source after transfer using the cryogenic defect distribution.

cases; with little difference between the two. This indicates that defects with longer time constants are the primary cause of CTI at these clocking rates, which is as expected since the transfer time is far apart from the typical divacancy emission time constant at this temperature. This is also shown by the cryogenic case performing slightly worse for this clocking scheme; corresponding to the higher density of defects with long emission time constants.

The short parallel scheme shows significantly more deferred charge; which is expected since the transfer time
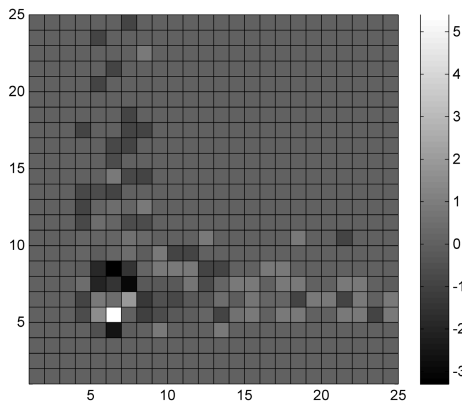
Fig. 7. Plot of the difference in electrons on a linear scale for the point source in the room-temperature case subtracted from the point source in the cryogenic case. This shows the increased spreading in the parallel direction for the cryogenic case, and the increased spreading in the serial direction for the room-temperature case.

is now closer to the divacancy emission time constant. The room-temperature case performs noticeably worse for this scheme; with approximately three times more deferred signal found in the first extended pixel. This corresponds to the much greater concentration of divacancy defects in this case. The serial scheme shows little difference in the FPR between the room-temperature and cryogenic cases, but approximately two times more deferred charge is found in the first extended pixel for the room-temperature case. This again shows the effect of the greater density of faster defects arising from a room-temperature irradiation.

A second test was performed using a point source with a Gaussian filter, which was transferred in both the parallel (short clocking scheme) and serial directions. The results are shown in Figs. 5 and 6. It can be seen that the results match those from the first test; with greater charge spreading in the parallel direction for the cryogenic case, and greater spreading in the serial direction for the room-temperature case. These simulations therefore give an example of the impact on imaging performance of the different defect distributions formed in a device irradiated at room-temperature and one irradiated at cryogenic temperature. Depending on the nominal temperature and clock timings the effect can be significant, which shows the potential importance of cryogenic irradiation studies for device characterization.

VI. CONCLUSION

Using the method of trap pumping we have studied radiation induced defects in a p-channel CCD irradiated with protons at 153 K. The defect emission time constants have been calculated at various time intervals both immediately following irradiation and after subsequent anneal phases up until a total anneal time of approximately 10 months. This has allowed for the analysis of longer term effects of such an irradiation on the defects formed within the device.

Calculation of the defect energy levels show that the dominant charge capturing defect under our operating conditions and postanneal is the donor level of the silicon divacancy, with a calculated energy level of $E_v + 0.20(\pm 0.02)$ eV. Also present is a carbon interstitial defect with an energy

$E_v + 0.26(\pm 0.02)$ eV. This is consistent with the defect distribution formed with a room-temperature irradiation, however, the dominant divacancy species only appears in the cryogenic case after the first room-temperature anneal. A key question for further work is the defect distribution in a device irradiated and kept at cryogenic temperature without further room-temperature anneal.

While the energy distributions show two dominant defect species, the emission time-constant distributions as well as the defect densities and locations show dynamic changes over these time scales. In particular more than one peak is observed in both the divacancy and carbon interstitial time-constant distributions at various times. Further investigation is therefore required in this area, such as analysis of any field or temperature dependencies of individual peaks. We also see small changes in the total number of defects within our detectable range right up until the final anneal stage.

The importance of cryogenic irradiation and annealing studies as opposed to the more standard technique of irradiating at room-temperature is apparent both because of the large differences in initial defect distributions and because of the major changes taking place during each anneal stage. It is also evident that if for a p-channel CCD a cryogenic irradiation results in a more favorable defect distribution than for the room-temperature case, then the device must be kept cold in order to maintain this distribution. Precise knowledge of defect parameters is vital in order to mitigate for radiation-induced CTI and so further analysis in this area provides scope for improved radiation tolerance of space-based detectors.

To analyze the potential impact of the different defect distributions which are produced for irradiation at room-temperature and at cryogenic temperature a model of charge transfer in a radiation damaged CCD was utilized. By simulating the effects of each distribution separately on both a 5-pixel block of charge and a Gaussian point source a comparison between the imaging performance in each case was obtained. It is shown that for certain temperatures and clocking schemes the effect can be significant, further stressing the importance of cryogenic irradiation studies for characterization, particularly in the context of space missions.

Throughout this paper, we have considered only p-channel devices, and hence only hole traps. In n-channel devices, which remain the current standard for space-based detectors, similar studies into the effects of a cryogenic irradiation on the electron trap distribution are ongoing [19]–[21].

REFERENCES

[1] G. Watkins, "Intrinsic defects in silicon," *Mater. Sci. Semicond. Process.*, vol. 3, no. 4, pp. 227–235, Aug. 2000.

[2] R. Massey *et al.*, "Pixel-based correction for charge transfer inefficiency in the *Hubble* space telescope advanced camera for surveys," *Monthly Notices Roy. Astron. Soc.*, vol. 401, pp. 371–384, Jan. 2010.

[3] J. Rhodes *et al.*, "The effects of charge transfer inefficiency (CTI) on galaxy shape measurements," *Pub. Astron. Soc. Pacific*, vol. 122, no. 890, pp. 439–450, Apr. 2010.

[4] J. P. D. Gow, N. J. Murray, A. D. Holland, and D. Burt, "Proton damage comparison of an e2v technologies n-channel and p-channel CCD204," *IEEE Trans. Nucl. Sci.*, vol. 61, no. 4, pp. 1843–1848, Aug. 2014.

[5] P. M. Mooney, L. J. Cheng, M. Süli, J. D. Gerson, and J. W. Corbett, "Defect energy levels in boron-doped silicon irradiated with 1-MeV electrons," *Phys. Rev. B, Condens. Matter*, vol. 15, no. 8, pp. 3836–3843, Apr. 1977.

[6] M. Asghar, M. Z. Iqbal, and N. Zafar, "Study of alpha-radiation-induced deep levels in *p*-type silicon," *J. Appl. Phys.*, vol. 73, no. 9, pp. 4240–4247, May 1993.

[7] A. Hallén, N. Keskitalo, F. Masszi, and V. Nágl, "Lifetime in proton irradiated silicon," *J. Appl. Phys.*, vol. 79, no. 8, pp. 3906–3914, Apr. 1996.

[8] C. A. Londos, "Deep-level transient spectroscopy studies of the interstitial carbon defect in silicon," *Phys. Rev. B, Condens. Matter*, vol. 35, no. 12, pp. 6295–6297, Apr. 1987.

[9] A. R. Frederickson, A. S. Karakashian, P. J. Drevinsky, and C. E. Caefer, "Radiation-induced carbon-related defects in *p*-type silicon," *J. Appl. Phys.*, vol. 65, no. 8, pp. 3272–3273, Apr. 1989.

[10] N. J. Mostek, C. J. Bebek, A. Karcher, W. F. Kolbe, N. A. Roe, and J. Thacker, "Charge trap identification for proton-irradiated p+ channel CCDs," *Proc. SPIE*, vol. 7742, p. 774216, Jul. 2010.

[11] D. Wood, D. J. Hall, J. Gow, N. Murray, K. Stefanov, and A. Holland, "Evolution of proton-induced defects in a cryogenically irradiated p-channel CCD," *Radiat. Effects Compon. Syst.*, to be published.

[12] W. Shockley and W. T. Read, Jr., "Statistics of the recombinations of holes and electrons," *Phys. Rev.*, vol. 87, no. 5, pp. 835–842, Sep. 1952.

[13] R. N. Hall, "Electron-hole recombination in germanium," *Phys. Rev.*, vol. 87, no. 2, p. 387, Jul. 1952.

[14] D. J. Hall, N. J. Murray, A. D. Holland, J. Gow, A. Clarke, and D. Burt, "Determination of *in situ* trap properties in CCDs using a 'single-trap pumping' technique," *IEEE Trans. Nucl. Sci.*, vol. 61, no. 4, pp. 1826–1833, Aug. 2014.

[15] N. J. Murray *et al.*, "Mitigating radiation-induced charge transfer inefficiency in full-frame CCD applications by 'pumping' traps," *Proc. SPIE*, vol. 8453, p. 845317, Jul. 2012.

[16] D. V. Lang, "Deep-level transient spectroscopy: A new method to characterize traps in semiconductors," *J. Appl. Phys.*, vol. 45, no. 7, pp. 3023–3032, Jul. 1974.

[17] J. Gow *et al.*, "Initial results from a cryogenic proton irradiation of a p-channel CCD," *Proc. SPIE*, vol. 9601, p. 96010F, Aug. 2015.

[18] J. Skottfelt, D. Hall, J. Gow, N. Murray, A. Holland, and T. Prod homme, "Comparing simulations and test data of a radiation damaged CCD for the Euclid mission," *J. Astron. Telescopes, Instrum., Syst.*, vol. 3, no. 2, p. 028001, Apr. 2017.

[19] N. Bush *et al.*, "The impact of radiation damage on photon counting with an EMCCD for the WFIRST-AFTA coronagraph," *Proc. SPIE*, vol. 9605, p. 96050E, Sep. 2015.

[20] L. K. Harding *et al.*, "Technology advancement of the CCD201-20 EMCCD for the WFIRST coronagraph instrument: Sensor characterization and radiation damage," *J. Astron. Telescopes, Instrum., Syst.*, vol. 2, no. 1, p. 011007, Dec. 2015.

[21] L. K. Harding *et al.*, "Electron multiplication CCD detector technology advancement for the WFIRST-AFTA coronagraph," *Proc. SPIE*, vol. 9605, p. 96050F, Sep. 2015.